





# Gamma-Ray Observations of Galaxy Clusters Strongly Constrain Dark Matter Annihilation in Prompt Cusps

Milena Crnogorčević <sup>1,\*</sup> M. Sten Delos <sup>2,†</sup> Nadia Kuritzén <sup>1,3,‡</sup> and Tim Linden <sup>1,§</sup>

<sup>1</sup>Stockholm University and The Oskar Klein Centre for Cosmoparticle Physics, Alba Nova, 10691 Stockholm, Sweden

<sup>2</sup>Carnegie Observatories, 813 Santa Barbara Street, Pasadena, CA 91101, USA

<sup>3</sup>The Viktor Rydberg Schools Foundation and Viktor Rydberg Gymnasium Odenplan, Frejgatan 30, 11349 Stockholm, Sweden

Thermal dark matter models generically include the prompt creation of highly-concentrated dark matter cusps in the early Universe. Recent studies find that these cusps can survive to the present day, as long as they do not fall into extremely dense regions of baryonic structure. In this work, we build models of dark matter annihilation within the prompt cusps that reside in galaxy clusters, showing that they dominate the total  $\gamma$ -ray annihilation signal. Using 15 years of *Fermi*-LAT data, we find no evidence for a  $\gamma$ -ray excess from these sources, and set strong constraints on annihilating dark matter. These constraints generically rule out the thermal annihilation cross-section to the  $b\bar{b}$  channel for dark matter masses below  $\sim 200$  GeV.

## I. INTRODUCTION

In standard cosmological models, “prompt cusps” of high dark matter density may efficiently form during certain phases in the early Universe [1–12] — a finding recently supported by novel analytical calculations [13, 14]. Intriguingly, studies indicate that these cusps, which follow a  $\rho_{\text{cusp}} \propto r^{-1.5}$  radial density profile, form almost instantaneously [15–17] and survive both halo growth [16] and clustering [18].

Although dense cusps represent only a small fraction of the total dark matter content of the Universe, their high densities lead them to dominate the dark matter annihilation signature in models where dark matter can annihilate [18–21]. Consequently, prompt cusps can greatly boost the flux of Standard Model particles, including photons, charged cosmic rays, and neutrinos, produced by dark matter annihilation, while also significantly altering the spatial distribution of this flux. In regions where prompt cusps drive the annihilation rate, the annihilation morphology tracks the number of prompt cusps, effectively tracing the dark matter density,  $\rho$ . This contrasts with typical annihilation signals, which scale with the square of dark matter density,  $\rho^2$ , and instead more closely resembles the signal expected from decaying dark matter.

The similarity between annihilation in prompt cusps and dark matter decay motivates  $\gamma$ -ray observations of galaxy clusters. As the most massive structures in the Universe, galaxy clusters stand among the best targets for the indirect detection of dark matter decay [22–29]. Notably, galaxy cluster constraints on decaying dark matter can set lower-limits on the dark matter lifetime that exceed  $10^{27}$  s [29].

Our analysis leverages the enhanced annihilation rate from prompt cusps to improve the sensitivity of  $\gamma$ -ray searches for dark matter. Most studies focus on  $\gamma$ -ray fluxes that scale with the square of dark matter density, favoring targets with high central densities, such as the Galactic Center [33–41] or dwarf spheroidal galaxies (dSphs) [31, 42–56]. However, the anni-

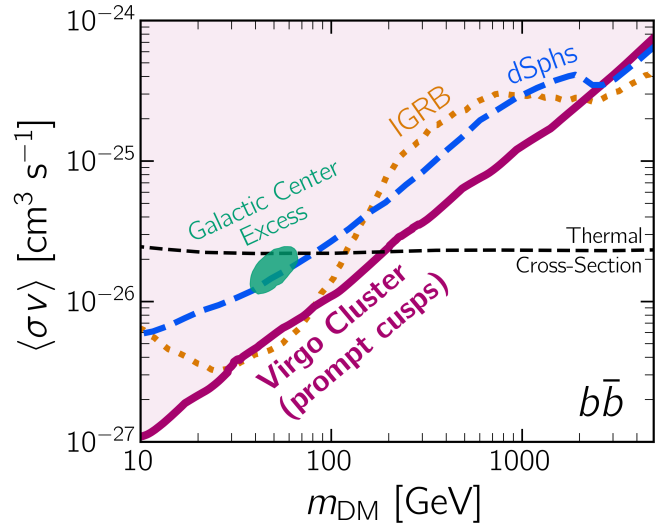


FIG. 1. Upper limits on the dark matter annihilation cross-section to a  $b\bar{b}$  final state in the Virgo cluster. Our limits (magenta solid) rule out the thermal annihilation cross-section (black dashed) for dark matter masses below 200 GeV [30], exceeding constraints from the stacking of dwarf spheroidal galaxies [31] (blue dashed) and from the IGRB [32] (orange dashed). These results are in tension with dark matter explanations for the Galactic Center Excess (green region) [33]. The light-shaded region indicates the excluded parameter space.

hilation rate from prompt cusps linearly depends on the total dark matter mass, elevating high mass targets (*e.g.*, galaxy clusters or the isotropic  $\gamma$ -ray background (IGRB) [32]), to the most promising candidates.

In this *paper*, we search for dark matter signals in the prompt cusps in galaxy clusters. First, we construct new models for the dark matter flux and morphology from seven nearby clusters, including Virgo, Centaurus, NGC 4636, M 49, Fornax (NGC 1399), Hydra, and Coma, accounting for both the internal density structure and spatial distribution of prompt cusps. We then analyze 15 years of  $\gamma$ -ray data from the *Fermi* Large Area Telescope (*Fermi*-LAT), finding no  $\gamma$ -ray excesses consistent with prompt cusp models. Figure 1 shows that observations of Virgo alone set a constraint on the dark matter annihilation cross section that is significantly stronger than previous limits from dSphs and the IGRB.

\* milena.crnogorcevic@fysik.su.se

† mdelos@carnegiescience.edu

‡ nadia.kuritzen@gmail.com

§ linden@fysik.su.se

The paper is organized as follows. In Section II, we characterize the annihilation signal from galaxy clusters, including the cosmological distribution of prompt cusps and the impact of tidal stripping. We then apply these models to specific clusters and compute the expected  $\gamma$ -ray flux. In Section III, we present our data analysis methodology and the statistical techniques employed to search for the  $\gamma$ -ray annihilation signal. We present our results in Section IV and compare our findings with existing constraints. Finally, we conclude in Section V.

## II. CHARACTERIZING THE ANNIHILATION SIGNAL

The prompt cusps that dominate the annihilation signal form around redshift  $z \sim 30$  [18] and later accrete onto the galaxy cluster halos that we target. Our calculation of cluster halo annihilation signatures thus proceeds in two parts. First, we describe the average distribution of prompt cusps within an arbitrary volume of dark matter. Next, we specialize to clusters, accounting for their spatial structure and the disruptive effects that occur therein.

### A. Cosmological distribution of prompt cusps

Prompt cusps form from local maxima in the initial density field. Each of these density peaks has a collapse time  $a_{\text{coll}}$ , which we estimate using the ellipsoidal collapse approximation in Ref. [57], and a characteristic comoving size  $R \equiv |\delta/\nabla^2\delta|^{1/2}$ , where  $\delta$  is the height of the peak in the density contrast and  $\nabla^2\delta$  is the Laplacian of the density contrast with respect to the comoving position. Numerical simulations [15–17] show that a peak with these parameters collapses to form a power-law cusp with profile  $\rho = Ar^{-1.5}$ , where:

$$A \simeq 24\bar{\rho}(a_{\text{coll}})(a_{\text{coll}}R)^{1.5}. \quad (1)$$

Here  $\bar{\rho}(a)$  is the cosmic mean dark matter density at the scale factor  $a$ . This profile initially extends out to the radius

$$r_{\text{cusp}} \simeq 0.11a_{\text{coll}}R. \quad (2)$$

These prompt cusps grow halos around them over time, and the halos also contribute to dark matter annihilation. However, prior halo and subhalo modeling suggests that their contribution to the annihilation rate is only at about the 10 percent level [18], so we neglect them.

Since the annihilation rate arising from a  $\rho \propto r^{-1.5}$  density cusp diverges at small radii, it is also important to understand the deep interior structure of a prompt cusp. Analytic arguments [16] (approximately confirmed in simulations [58]) require that the initial thermal motion of the dark matter give rise to a finite-density core of radius

$$r_{\text{core}} \simeq 0.34G^{-2/3}(m_{\text{DM}}/T_{\text{d}})^{-2/3}\bar{\rho}(a_{\text{d}})^{-4/9}A^{-2/9}, \quad (3)$$

where  $m_{\text{DM}}$  is the dark matter particle mass,  $T_{\text{d}}$  is the temperature at which the dark matter kinetically decouples from the Standard Model plasma, and  $\bar{\rho}(a_{\text{d}})$  is the dark matter density at the time of kinetic decoupling [18]. Note that typically

$r_{\text{core}} \sim 10^{-3}r_{\text{cusp}}$ . Assuming that the  $\rho = Ar^{-1.5}$  density profile transitions abruptly into a constant-density core at the radius  $r_{\text{core}}$ , the annihilation rate from radii below  $r_{\text{cusp}}$  is proportional to the quantity

$$j \equiv \int_{\text{cusp}} \rho^2 dV = 4\pi A^2 [1/3 + \ln(r_{\text{cusp}}/r_{\text{core}})]. \quad (4)$$

More realistic models of the central core lead to a slightly higher annihilation rate [59].

The cosmological distribution of prompt cusps follows directly from the distribution of peaks in the initial density field, which is a well understood mathematical problem [60]. To describe the initial density field, we fix a dark matter power spectrum using the procedure described by Refs. [18, 21, 32]. We begin by evaluating the dark matter power spectrum at  $z = 31$  using CLASS [61] with cosmological parameters from the Planck mission [62], and we extrapolate it beyond the code's numerical resolution limit using the analytic solution of Ref. [63] that is valid in the small-scale limit. The result is the spectrum of initial density variations for an idealized cold dark matter model, but in practice, the thermal motion of the dark matter suppresses inhomogeneities on smaller scales than the distances that particles randomly stream. The free-streaming scale depends on the dark matter model, namely its mass  $m_{\text{DM}}$  and decoupling temperature  $T_{\text{d}}$  (which is set by its elastic interactions with the Standard Model). We consider a range of models, and for each one, we evaluate the free-streaming wavenumber  $k_{\text{fs}}$  according to Ref. [64] and scale the power spectrum by  $e^{-k^2/k_{\text{fs}}^2}$ . Prompt cusps arise from density perturbations with length scales of order  $k_{\text{fs}}^{-1}$ .

With the power spectrum set, we follow the approach of Ref. [18] to evaluate the statistics of initial peaks and to translate this into the cosmological abundance and distribution of prompt cusps. The procedure is to evaluate the comoving number density  $n_{\text{peaks}}$  of initial peaks and to randomly sample the properties of  $10^7$  of them. Any mass  $M$  of dark matter contains an average of  $Mn_{\text{peaks}}/\bar{\rho}_0$  initial peaks, where  $\bar{\rho}_0 \simeq 33 M_{\odot} \text{kpc}^{-3}$  is the comoving dark matter density. If we associate each peak with a cusp that contributes some  $j$  to the annihilation rate, in accordance with Eq. (4), then these cusps would contribute in total

$$\int_{\text{cusps}} \rho^2 dV = Mn_{\text{peaks}}\langle j \rangle/\bar{\rho}_0, \quad (5)$$

where angle brackets indicate the average. The average contribution of the prompt cusps per mass of dark matter is:

$$\rho_{\text{eff},0} \equiv \frac{\int_{\text{cusps}} \rho^2 dV}{M} = n_{\text{peaks}}\langle j \rangle/\bar{\rho}_0. \quad (6)$$

For a dark matter particle of mass  $m_{\text{DM}}$  and cross section  $\langle\sigma v\rangle$  (which we assume to be velocity-independent at lowest order), the cusps would contribute an average annihilation rate

$$\left\langle \frac{\Gamma}{M} \right\rangle_0 = \frac{\langle\sigma v\rangle}{2m_{\text{DM}}^2} \rho_{\text{eff},0} \quad (7)$$

per mass of dark matter.

So far, we have assumed that each initial peak can be associated with a prompt cusp with density profile given by Eqs (1-3), which is why we use the subscript ‘0’ in Eqs. (6) and (7). This assumption does not fully hold. Some initial peaks do not collapse to form prompt cusps because they accrete into previously formed structures first. Additionally, some of the prompt cusps that do form are destroyed in halo mergers. The approximate picture is that when a small halo accretes onto a much larger halo, the small halo persists as a subhalo, and the central cusps of both halos survive. On the other hand, when halos of comparable mass merge, dynamical friction causes their central cusps to also merge, and this process decreases the number of prompt cusps (and the inner structure of the central cusp of the larger halo is only slightly altered [16]). Based on the simulations of Ref. [16], Ref. [18] estimated that due to these effects, only about half of the initial density peaks produce prompt cusps that persist today. These surviving cusps contribute a fraction  $f_{\text{surv}}$  of the annihilation signal predicted by Eq. (6), where  $f_{\text{surv}} \simeq 0.5 \pm 0.1$ . We will adopt  $f_{\text{surv}} = 0.5$ .

### B. Annihilation in galaxy clusters

Now, we consider a cluster halo with density profile  $\rho(r)$ . Let  $dN_\gamma/dE$  be the spectrum of  $\gamma$ -ray photons produced by each dark matter annihilation event. The differential photon flux (per solid angle) received by an observer is then

$$\frac{d^2\Phi}{d\Omega dE} = \frac{1}{4\pi} \frac{dN_\gamma}{dE} \int_0^\infty d\ell \rho(r) \left\langle \frac{\Gamma}{M} \right\rangle, \quad (8)$$

given in terms of the annihilation rate per mass of dark matter,  $\langle \Gamma/M \rangle$ . Here,  $\ell$  is the position along the observer’s line of sight, and the cluster-centric radius  $r$  accordingly depends on  $\ell$ . We expand the annihilation rate as

$$\left\langle \frac{\Gamma}{M} \right\rangle = \frac{\langle \sigma v \rangle}{2m_{\text{DM}}^2} [\rho(r) + f_{\text{surv}} f_{\text{tidal}}(r) \rho_{\text{eff},0}]. \quad (9)$$

The first term represents the smooth halo, which contains almost all of the dark matter, as only about 1% resides in prompt cusps [18]. The second term accounts for the cusps and is constructed by scaling Eq. (7) by the cusp survival factor  $f_{\text{surv}}$  and by a position-dependent factor  $f_{\text{tidal}}(r)$ .

Inside the halo of a galaxy cluster, prompt cusps are gradually stripped by tidal forces. To account for this effect, we employ the model of Ref. [65], which uses the tidal field at a subhalo’s orbital pericenter to predict the density profile of its asymptotic remnant after an arbitrarily long period of tidal stripping. For cusps at a radius  $r$  within a cluster, we make a simple approximation that the pericenter radii  $r_p$  are uniformly distributed between  $r_p = 0$  and  $r_p = r$ . Appendix A shows that this is a reasonable approximation. For each cusp sampled in Section II A, which had the initial annihilation rate coefficient  $j$  given by Eq. (4), we can evaluate a new coefficient  $j' = \int \tilde{\rho}^2 dV$  associated with the cusp’s tidally evolved density profile  $\rho'$ . We then define

$$f_{\text{tidal}}(r) = \langle j' \rangle / \langle j \rangle, \quad (10)$$

Name	RA, Dec (deg.)	$J$ ( $\text{GeV}^2 \text{cm}^{-5}$ )	distance
Virgo	187.70, 12.34	$8.88 \times 10^{20}$	$17.053 \pm 0.360$
NGC 4636	190.71, 2.69	$6.85 \times 10^{19}$	$16.303 \pm 0.578$
Hydra	139.53, -12.09	$4.99 \times 10^{19}$	$245.41 \pm 17.25$
Coma	194.95, 27.98	$4.95 \times 10^{19}$	$109.350 \pm 8.261$
M49	187.44, 8.00	$4.88 \times 10^{19}$	$16.060 \pm 0.348$
Centaurus	192.20, -41.31	$4.61 \times 10^{19}$	$40.100 \pm 2.177$
Fornax	54.62, -35.45	$4.12 \times 10^{19}$	$17.711 \pm 0.395$

TABLE I. Clusters considered in our analysis. The annihilation  $J$  factor depends mildly on the dark matter mass and decoupling temperature; here we fix  $m_{\text{DM}} = 100$  GeV and  $T_d = 30$  MeV.

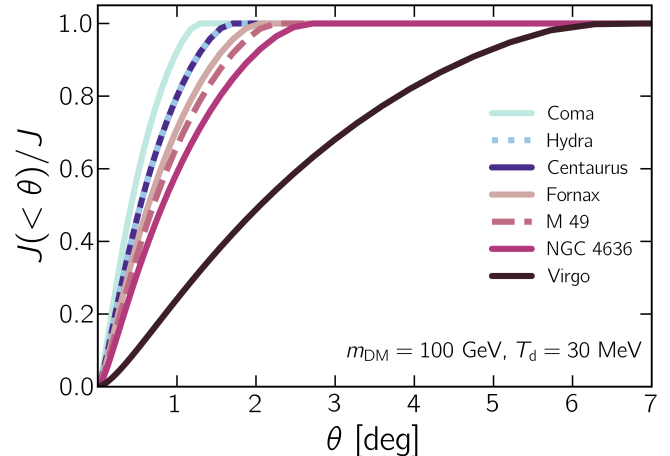


FIG. 2. Spatial extent of each cluster’s annihilation signal. For each angle  $\theta$  from the cluster center, we show the fractional contribution to the  $J$  factor that comes from angles less than  $\theta$ .

where the brackets average over the pericenter radii  $r_p < r$ .

We consider the clusters in Table I and adopt the density profiles  $\rho(r)$  and distances from Ref. [28]. From Eqs. (8) and (9), the differential photon flux from each cluster is:

$$\frac{d^2\Phi}{d\Omega dE} = \frac{\langle \sigma v \rangle}{8\pi m_{\text{DM}}^2} \frac{dN_\gamma}{dE} \frac{dJ}{d\Omega}, \quad (11)$$

where the spatial distribution of the dark matter is in the factor

$$\frac{dJ}{d\Omega} \equiv \int_0^\infty d\ell \rho(r) [\rho(r) + f_{\text{surv}} f_{\text{tidal}}(r) \rho_{\text{eff},0}]. \quad (12)$$

Integrated over solid angles, the total annihilation luminosity of a cluster is proportional to

$$J = \int d\Omega \frac{dJ}{d\Omega}. \quad (13)$$

Table I gives the annihilation  $J$  factor of each cluster for an example model with  $m_{\text{DM}} = 100$  GeV and  $T_d = 30$  MeV. Figure 2 shows the annihilation morphology over the sky. Due to its proximity, the Virgo cluster has the highest  $J$  by far, but it also produces the most spatially extended signal.

Generally, higher dark matter masses and earlier decoupling (higher  $T_d$ ) both lead to larger values of  $J$ , because

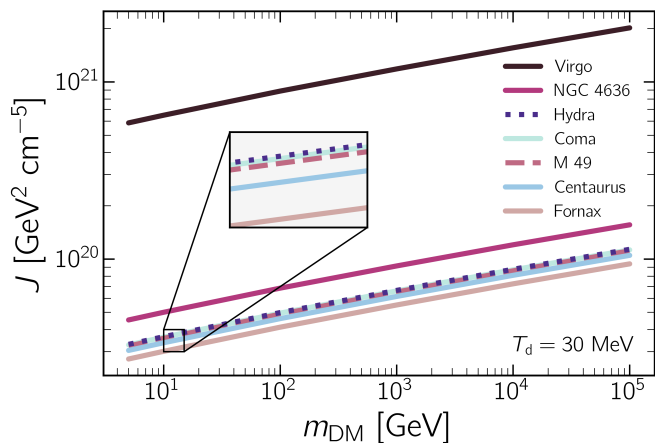


FIG. 3. Cluster  $J$  factors, shown as a function of the dark matter mass. Higher particle masses correspond to colder dark matter, so the prompt cusps are smaller and form at earlier times. The earlier formation makes these cusps more internally dense, resulting in a higher annihilation rate.

they cause the prompt cusps to be slightly more internally dense. However,  $J$  depends only logarithmically on  $m_{\text{DM}}$  and  $T_{\text{d}}$  [18]. We follow previous studies [32, 66] in fixing  $T_{\text{d}} = 30$  MeV for simplicity. This is a mildly conservative choice; lower  $T_{\text{d}}$  tend to be in tension with terrestrial experiments [67], since they require a strong kinetic coupling between the dark matter and the Standard Model. We however analyze a range of dark matter masses  $m_{\text{DM}}$ , and Fig. 3 shows how each cluster’s  $J$  factor varies with  $m_{\text{DM}}$  (with  $T_{\text{d}} = 30$  MeV fixed). The spatial distribution of the annihilation signal also depends in principle on  $m_{\text{DM}}$ , since denser cusps are less susceptible to tidal stripping. However, this variation is small enough that Fig. 2 does not discernibly change over the full range of  $5 \text{ GeV} < m_{\text{DM}} < 10^5 \text{ GeV}$ .

Figure 4 illustrates the different contributions to the  $J$  factor in Eq. (12). The total signal from the smooth halo is subdominant compared to the signal from the prompt cusps and only contributes nonnegligibly at angles smaller than about  $0.01^\circ$  from the cluster center. Such angles are far smaller than the angular resolution of the Fermi telescope. Tidal forces reduce the annihilation signal from the cusps by only about 5–10%.

### III. DATA ANALYSIS

The Large Area Telescope (LAT), onboard the *Fermi*  $\gamma$ -ray observatory, detects  $\gamma$  rays with energies spanning 20 MeV–500 GeV. Its field of view (FoV) covers  $\sim 20\%$  of the sky at all times, allowing full-sky coverage at a cadence of about 3 hours. Its source localization accuracy reaches a few arcminutes. The instrument paper provides a comprehensive overview of the LAT instrument and its performance [68].

We analyze 15 years of Pass 8 reprocessed data covering the period from August 4, 2008, to November 1, 2023, obtained from the *Fermi* Science Support Center (FSSC)

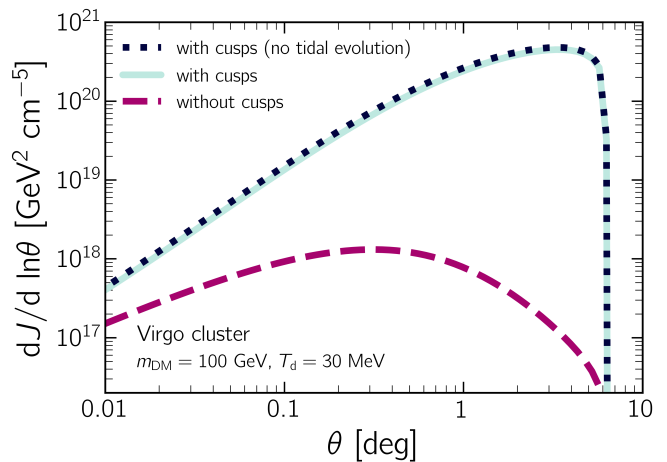


FIG. 4. Comparing different contributions to the annihilation signal of the Virgo cluster. As a function of the angle  $\theta$  from the cluster center, we show the contribution  $dJ/d \ln \theta = 2\pi\theta^2 dJ/d\Omega$  of each logarithmic angular interval to the integrated  $J$  factor. The light teal solid curve shows the net predicted  $J$  factor, which we use for our analysis. The navy dotted curve shows the  $J$  factor without accounting for tidal stripping of prompt cusps (5–10% higher). The magenta dashed curve shows the  $J$  factor from the smooth halo alone, neglecting contributions from cusps altogether.

website<sup>1</sup>. All data are analyzed using the *fermipy* software package (v. 1.2.0) [69], which relies on *FermiTools* (v. 2.2.0)<sup>2</sup> for likelihood-based modeling and fitting. We select photons from the P8R3\_SOURCE\_V3 event class with energies between 500 MeV and 500 GeV, spaced in 8 logarithmic bins in each decade in energy. We apply the standard models for the Galactic diffuse emission (*gll\_iem\_v07*) and the isotropic diffuse background (*iso\_P8R3\_SOURCE\_V3*), as provided by the *Fermi*-LAT Collaboration. For each source, we define a  $20^\circ \times 20^\circ$  region of interest (RoI), binned at  $0.2^\circ$  and centered on the cluster’s dynamical center. We model both the point and extended sources within the RoI using the 4FGL-DR3 catalog (*gll\_psc\_v29*), extending to  $25^\circ \times 25^\circ$  to account for photon leakage from the LAT point spread function. We introduce a zenith angle cut of  $90^\circ$  to account for possible contamination from the Earth’s limb and apply the standard good time interval (GTI) selection cuts.

After constructing the model, we perform a binned likelihood analysis for each source. The likelihood function compares models with and without an associated  $\gamma$ -ray source, quantifying the goodness of fit using the Test Statistic (TS), defined as  $TS = -2 \log(\mathcal{L}_0/\mathcal{L}_1)$ , where  $\mathcal{L}_0$  represents the likelihood of the null hypothesis (no signal), and  $\mathcal{L}_1$  is the likelihood of the alternative hypothesis (signal present). We perform an extended-source analysis using the dark-matter signal templates described in Sec. II for the seven clusters

<sup>1</sup> <https://fermi.gsfc.nasa.gov/ssc/data/>, accessed on January 19, 2025.

<sup>2</sup> <https://fermi.gsfc.nasa.gov/ssc/data/analysis/software/>, accessed on January 19, 2025.



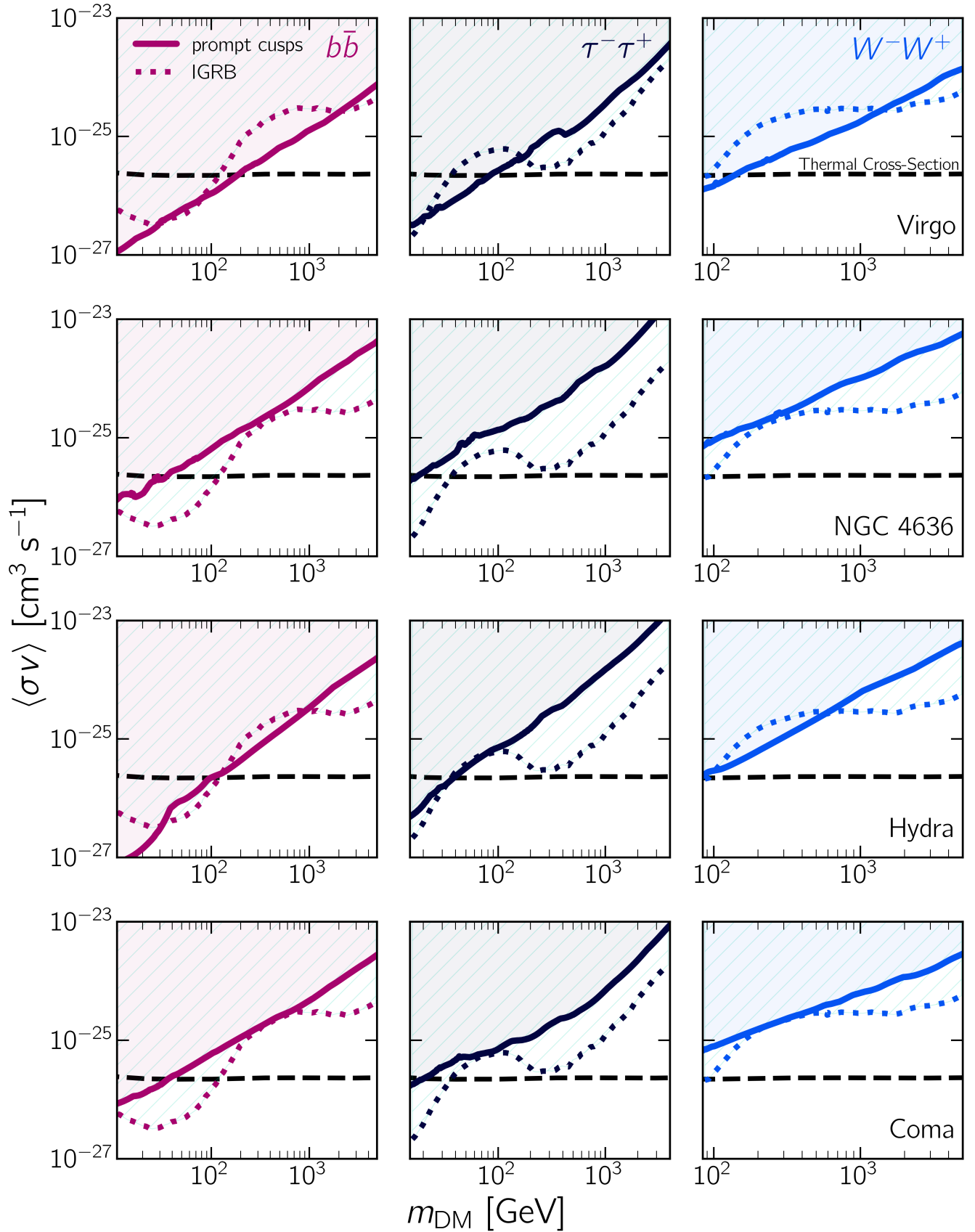


FIG. 5. Upper limits on the annihilation cross-section from our seven selected galaxy clusters as a function of dark matter mass, based on the extended source models discussed in Section II. We consider three annihilation channels:  $b\bar{b}$  (magenta),  $\tau^+\tau^-$  (navy), and  $W^+W^-$  (blue). We compare our results (solid lines) with previous upper limits from the studies of the IGRB (dotted lines), from Ref. [32]. The canonical thermal annihilation cross-section is shown as black dashed line [30]. The light-shaded regions represent the parameter space excluded by galaxy cluster observations, while the hatched regions indicate exclusions based on the IGRB analysis. We find that Virgo constraints are typically the strongest, ruling out dark matter annihilating at the thermal cross-section for masses up to 200 GeV, 88 GeV, and 147 GeV for annihilations to  $b\bar{b}$ ,  $\tau^+\tau^-$ , and  $W^+W^-$ , respectively.

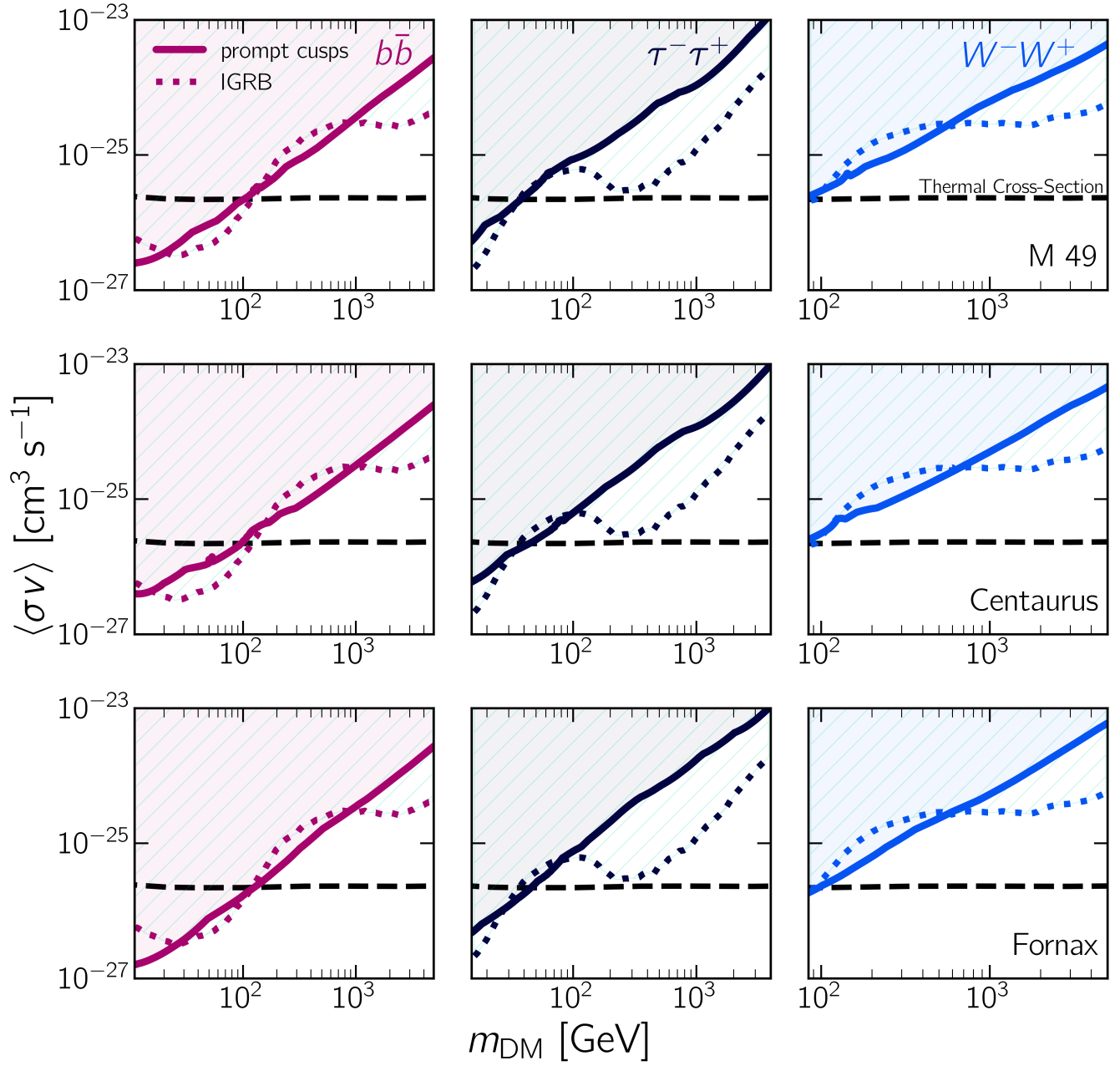


FIG. 5 continued.

from Table I. We model the dark matter profile from each cluster out to  $6^\circ$  from the cluster center, in order to model the entire dark matter contribution (see Figure 2). For each cluster, we use the `gta.sed()` module in `fermipy` to estimate the source flux by fitting the spectrum in each energy bin assuming a power-law shape with an index of 2. This method also produces a spectral energy distribution (SED) curve, and energy flux  $E^2 dN/dE$ , along with a corresponding delta log-likelihood profile,  $\Delta\mathcal{L}(d\Phi_\gamma/dE, E)$ . Once the flux (or upper limit) is determined, we translate the SEDs into dark matter constraints. The  $\gamma$ -ray flux from dark matter annihilation is:

$$\frac{d\Phi_\gamma}{dE} = \frac{1}{8\pi} \frac{\langle\sigma v\rangle}{m_{\text{DM}}^2} \frac{dN}{dE} \times J(m_{\text{DM}}), \quad (14)$$

where  $\langle\sigma v\rangle$  is the velocity-weighted annihilation cross-section,  $m_{\text{DM}}$  is the mass of the dark matter particle, and  $dN/dE$  is the spectrum of  $\gamma$  rays produced per annihilation event (depending on the dark matter mass and annihilation channel) [70]. Finally, we are then able to constrain the dark matter parameter space by calculating  $TS$  values for each combination of cross-section and mass,

$$TS(\langle\sigma v\rangle, m_{\text{DM}}) = -2 \log \frac{\mathcal{L}_0}{\mathcal{L}(\langle\sigma v\rangle, m_{\text{DM}})} \quad (15)$$

where  $\mathcal{L}_0$  is the likelihood of the null hypothesis (no dark matter) and  $\mathcal{L}(\langle\sigma v\rangle, M_\chi)$  represents the likelihood of the model with dark matter. We sample 1,000 logarithmically spaced dark matter masses between 10 GeV–10 TeV and 60,000  $\langle\sigma v\rangle$  values logarithmically spaced within 5 orders of magnitude around the thermal relic cross-section ( $3 \times 10^{-26}$  cm<sup>3</sup>/s) in both directions. We use  $J$  factors from Fig. 3 and annihilation channels that produce  $b\bar{b}$ ,  $\tau^+\tau^-$ , and  $W^+W^-$  final states. By stepping through the values of  $\langle\sigma v\rangle$ , we determine the cross-section value corresponding to a 95% confidence level (CL) limit, defined as the point where the  $TS$  value decreases by 2.71.

#### IV. RESULTS

We find no evidence for a spatially extended  $\gamma$ -ray signal in any of the seven galaxy clusters listed in Table I. Thus, we place upper limits on the dark matter annihilation cross section using 15 years of *Fermi*-LAT data.

The Virgo cluster, unsurprisingly, provides the strongest constraints among our targets, primarily due to its large annihilation  $J$ -factor (Fig. 3). Figure 1 compares our Virgo limits for the  $b\bar{b}$  annihilation channel to other relevant benchmarks, showing that we rule out dark matter masses below  $\sim 200$  GeV at a 95% CL. Below  $\sim 1$  TeV, our Virgo limit is stronger by about an order of magnitude compared to the stacking of dwarf spheroidal galaxies, while at higher masses (up to  $\sim 10$  TeV) it remains competitive [31]. Finally, our annihilation limits are about an order of magnitude more stringent than previous limits from galaxy clusters [28] and the broader large-scale structure [71], which relied on conventional subhalo models that did not account for prompt cusps.

Figure 5 shows our results for annihilation into  $b\bar{b}$ ,  $\tau^+\tau^-$  and  $W^+W^-$ . Besides Virgo, our sample includes Centaurus, NGC 4636, M 49, Fornax (NGC 1339), Hydra, and Coma. For the  $b\bar{b}$  channel, our limits exclude the thermal relic cross section for dark matter in the  $\sim 20$ – $200$  GeV mass range. At higher masses, we observe the sensitivity fall-off characteristic of  $\gamma$ -ray searches, where the decreasing photon statistics weaken the constraints above a few hundred GeV. Finally, although these clusters have lower  $J$ -factors (Fig. 3), their smaller spatial extension leads to upper limits that are within an order of magnitude of the Virgo constraints. This strengthens our conclusion by showing that any issue with Virgo (*e.g.*, a complex merger history) does not strongly affect our results.

#### V. CONCLUSION

Our results strongly constrain dark matter annihilation in standard cosmological models. The prompt cusps that arise in these scenarios constitute only a small fraction of the dark matter mass, but they dominate the annihilation rate today. We find that, for dark matter masses below a few hundred GeV (annihilating into hadronic final states), our limits from prompt cusps in the Virgo cluster represent the most stringent bounds to date, surpassing those from dSphs and the IGRB. This improvement arises because the annihilation rate in these cusps scales with  $\rho$ , rather than  $\rho^2$ , and is therefore enhanced in massive, extended structures such as galaxy clusters.

These new limits exclude regions of the thermal WIMP parameter space that would remain allowed under conventional substructure assumptions. While typical astrophysical searches focus on centrally dense targets like the Galactic Center or dSphs, our work underscores the crucial role that galaxy clusters can play when prompt cusps are taken into account. Moreover, these constraints, derived under standard cosmological assumptions, not only exceed those from dwarf galaxies but also strongly disfavor the dark matter interpretation of the Galactic Center Excess. This comparison is appropriate, as prompt cusps would not boost annihilation to a significant degree in those already-dense regions [18, 59].

Furthermore, our results usually provide stronger constraints on dark matter annihilation compared to the IGRB constraints on prompt cusps analyzed in [32]. While Delos *et al.* exclude dark matter masses below  $\sim 120$  GeV for annihilation into  $b\bar{b}$ , we extend this exclusion up to  $\sim 200$  GeV by focusing on galaxy clusters. This improvement is due to our targeting of high  $J$ -factor regions where the annihilation signal is enhanced compared to the diffuse IGRB.

Finally, the highly extended, but not entirely isotropic, nature of galaxy cluster searches remains tractable (if challenging) for next-generation atmospheric Cherenkov telescopes, as well as future MeV instruments. Moving forward, extending this analysis to include next-generation  $\gamma$ -ray observatories with improved sensitivity and angular resolution will be crucial for further probing the dark matter parameter space. These efforts will not only refine our understanding of dark matter, but also strengthen the synergy between observational and theoretical studies in astrophysics and particle physics.

## ACKNOWLEDGEMENTS

MC and TL acknowledge support from the Swedish Research Council under contract 2022-04283 and the Swedish National Space Agency under contract 2023-00242.

This project made use of Astropy [72], Numpy [73], Matplotlib [74], and Pandas [75] Python packages. The authors also acknowledge the use of public data from the *Fermi Science Support Center* data archive. Figure preparation was supported by resources made available by Ciaran O’Hare at <https://github.com/cajohare/HowToMakeAPlot> (last accessed on January 20, 2025). The color scheme used in our plots was inspired by *Cooper & Gorfer - “The Garden,”* exhibited at the Fotografiska Museum in Stockholm in 2021.

### Appendix A: Pericenter distribution

In Sec. II, we assumed that cusp orbital pericenters are uniformly distributed in radius. Here we evaluate the pericenter distribution for idealized halos and show that the pericenter radius distribution is indeed close to uniform. For this purpose, consider a halo with an isotropic distribution function  $f_{\text{DF}}(E)$ . That implies that at any fixed radius  $r$ , the velocity distribution is

$$dP = \frac{f_{\text{DF}}(\Phi(r) + \mathbf{v}^2/2)}{\rho(r)} d^3\mathbf{v}, \quad (\text{A1})$$

where  $\Phi(r)$  is the gravitational potential and  $\rho(r)$  is the density profile. We write this distribution as a differential probability  $dP$ , a useful representation as we transform the distribution to other variables.

Now consider the velocity in spherical coordinates aligned along the radius vector, taking  $\theta$  to be the angle between  $\mathbf{v}$  and  $\mathbf{r}$ , so that  $d^3\mathbf{v} = 2\pi d\cos\theta v^2 dv$ . Here we integrate out the azimuthal angle, since it is irrelevant to the calculation. The polar angle  $\theta$  is relevant, however, because by conservation of energy and angular momentum, it is related to the pericenter radius  $r_p$  through

$$\Phi(r) - \Phi(r_p) - \left( \sin^2\theta \frac{r^2}{r_p^2} - 1 \right) \frac{v^2}{2} = 0. \quad (\text{A2})$$

By inserting a Dirac delta function  $\delta_D$  to enforce Eq. (A2) and appropriately scaling by the derivative of Eq. (A2) with

respect to  $r_p$ , we can expand the differential probability as

$$\begin{aligned} dP &= \frac{f_{\text{DF}}(\Phi(r) + v^2/2)}{\rho(r)} 2\pi d\cos\theta v^2 dv \\ &\times \delta_D \left\{ \Phi(r) - \Phi(r_p) - \left( \sin^2\theta \frac{r^2}{r_p^2} - 1 \right) \frac{v^2}{2} \right\} \\ &\times \left| \sin^2\theta \frac{r^2}{r_p^3} v^2 - \Phi'(r_p) \right| dr_p, \end{aligned} \quad (\text{A3})$$

where  $\Phi'$  is the derivative of the potential. To obtain the pericenter distribution, all that remains is to integrate out  $v$  and  $\theta$ . The  $\theta$  integral yields

$$\begin{aligned} dP &= \frac{f_{\text{DF}}(\Phi(r) + v^2/2)}{\rho(r)} 4\pi v^2 dv \\ &\times \theta_H \left[ v^2 - 2r_p^2 \frac{\Phi(r) - \Phi(r_p)}{r^2 - r_p^2} \right] \\ &\times \frac{r_p}{rv} \frac{|v^2 + 2(\Phi(r) - \Phi(r_p)) - r_p \Phi'(r_p)|}{\sqrt{(r^2 - r_p^2)v^2 - 2r_p^2(\Phi(r) - \Phi(r_p))}} dr_p, \end{aligned} \quad (\text{A4})$$

where the Heaviside step function  $\theta_H$  selects the velocities  $v$  for which Eq. (A2) has solutions. The distribution of pericenter radii  $r_p$  is thus

$$\begin{aligned} \frac{dP}{dr_p} &= \frac{4\pi r_p}{\rho(r)r} \int_{v_{\min}(r_p, r)}^{\infty} dv v f_{\text{DF}}(\Phi(r) + v^2/2) \\ &\times \frac{|v^2 + 2(\Phi(r) - \Phi(r_p)) - r_p \Phi'(r_p)|}{\sqrt{(r^2 - r_p^2)v^2 - 2r_p^2(\Phi(r) - \Phi(r_p))}}, \end{aligned} \quad (\text{A5})$$

where  $v_{\min}(r_p, r) \equiv \sqrt{2r_p^2[\Phi(r) - \Phi(r_p)]/(r^2 - r_p^2)}$ .

For a singular isothermal sphere, with distribution function  $f(E) = e^{-E/\sigma^2}/[(2\pi)^{5/2}G\sigma]$ , potential  $\Phi(r) = 2\sigma^2 \ln(r)$ , and density profile  $\rho(r) = \sigma^2/(2\pi G r^2)$  (for some set velocity dispersion  $\sigma$ ), the pericenter distribution can be evaluated analytically, yielding

$$\frac{dP}{dr_p} = \frac{[4 \ln(r/r_p) - 1]r^2 + r_p^2}{(r^2 - r_p^2)^{3/2}} \left( \frac{r_p}{r} \right)^{\frac{r^2 + r_p^2}{r^2 - r_p^2}}. \quad (\text{A6})$$

We show this distribution as the black curve in Fig. 6. For a more realistic NFW density profile, we evaluate the pericenter distribution numerically using the distribution function given as a fitting function by Ref. [76]. For several radii  $r$ , we show the resulting pericenter distributions as the colored curves in Fig. 6.

[1] J. Diemand, M. Zemp, B. Moore, J. Stadel, and M. Carollo, *Mon. Not. Roy. Astron. Soc.* **364**, 665 (2005), [arXiv:astro-ph/0504215](https://arxiv.org/abs/astro-ph/0504215).  
[2] T. Ishiyama, J. Makino, and T. Ebisuzaki, *ApJ* **723**, L195 (2010), [arXiv:1006.3392](https://arxiv.org/abs/1006.3392) [astro-ph.CO].

[3] D. Anderhalden and J. Diemand, *JCAP* **04**, 009 (2013), [Erratum: *JCAP* 08, E02 (2013)], [arXiv:1302.0003](https://arxiv.org/abs/1302.0003) [astro-ph.CO].  
[4] T. Ishiyama, *Astrophys. J.* **788**, 27 (2014), [arXiv:1404.1650](https://arxiv.org/abs/1404.1650) [astro-ph.CO].  
[5] E. Polisensky and M. Ricotti, *MNRAS* **450**, 2172 (2015),



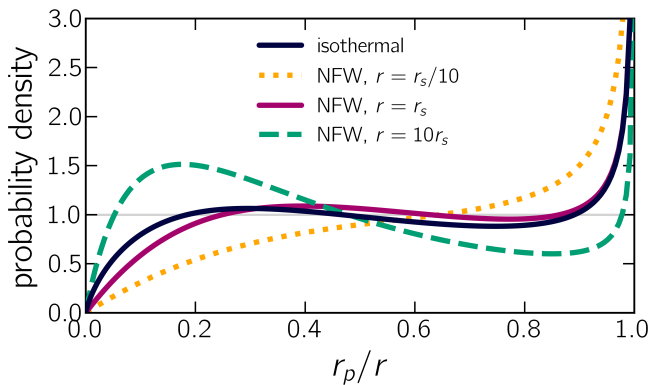


FIG. 6. Distributions of pericenter radii for particles in idealized halos. We consider an isothermal sphere (black curve) and particles at several set radii inside NFW halos with isotropic velocity distributions (colored curves). For reference, the thin horizontal line indicates a uniform distribution. The pericenter distributions tend to be close to uniform in radius.

- arXiv:1504.02126 [astro-ph.GA].
- [6] G. Ogiya, D. Nagai, and T. Ishiyama, *Mon. Not. Roy. Astron. Soc.* **461**, 3385 (2016), arXiv:1604.02866 [astro-ph.CO].
- [7] R. E. Angulo, O. Hahn, A. Ludlow, and S. Bonoli, *Mon. Not. Roy. Astron. Soc.* **471**, 4687 (2017), arXiv:1604.03131 [astro-ph.CO].
- [8] M. S. Delos, A. L. Erickcek, A. P. Bailey, and M. A. Alvarez, *Phys. Rev. D* **97**, 041303 (2018), arXiv:1712.05421 [astro-ph.CO].
- [9] M. S. Delos, A. L. Erickcek, A. P. Bailey, and M. A. Alvarez, *Phys. Rev. D* **98**, 063527 (2018), arXiv:1806.07389 [astro-ph.CO].
- [10] G. Ogiya and O. Hahn, *Mon. Not. Roy. Astron. Soc.* **473**, 4339 (2018), arXiv:1707.07693 [astro-ph.CO].
- [11] T. Ishiyama and S. Ando, *Mon. Not. Roy. Astron. Soc.* **492**, 3662 (2020), arXiv:1907.03642 [astro-ph.CO].
- [12] S. Colombi, *Astron. Astrophys.* **647**, A66 (2021), arXiv:2012.04409 [astro-ph.CO].
- [13] S. D. M. White, *Mon. Not. Roy. Astron. Soc.* **517**, L46 (2022), arXiv:2207.13565 [astro-ph.CO].
- [14] A. Del Popolo and S. Fakhry, *Phys. Dark Univ.* **41**, 101259 (2023), arXiv:2305.19817 [astro-ph.CO].
- [15] M. S. Delos, M. Bruff, and A. L. Erickcek, *Phys. Rev. D* **100**, 023523 (2019), arXiv:1905.05766 [astro-ph.CO].
- [16] M. S. Delos and S. D. M. White, *Mon. Not. Roy. Astron. Soc.* **518**, 3509 (2022), arXiv:2207.05082 [astro-ph.CO].
- [17] L. Ondaro-Mallea, R. E. Angulo, J. Stücker, O. Hahn, and S. D. M. White, *Mon. Not. Roy. Astron. Soc.* **527**, 10802 (2023), arXiv:2309.05707 [astro-ph.GA].
- [18] M. S. Delos and S. D. M. White, *JCAP* **10**, 008 (2023), arXiv:2209.11237 [astro-ph.CO].
- [19] C. Blanco, M. S. Delos, A. L. Erickcek, and D. Hooper, *Phys. Rev. D* **100**, 103010 (2019), arXiv:1906.00010 [astro-ph.CO].
- [20] M. S. Delos, T. Linden, and A. L. Erickcek, *Phys. Rev. D* **100**, 123546 (2019), arXiv:1910.08553 [astro-ph.CO].
- [21] M. S. Delos, *Phys. Rev. D* **109**, 023532 (2024), arXiv:2310.15214 [astro-ph.CO].
- [22] M. Ackermann, M. Ajello, A. Allafort, L. Baldini, J. Ballet, G. Barbiellini, D. Bastieri, K. Bechtol, and et al., *J. Cosmology Astropart. Phys.* **2010**, 025 (2010), arXiv:1002.2239 [astro-ph.CO].
- [23] X. Huang, G. Vertongen, and C. Weniger, *JCAP* **01**, 042 (2012), arXiv:1110.1529 [hep-ph].
- [24] S. Ando and D. Nagai, *J. Cosmology Astropart. Phys.* **2012**, 017 (2012), arXiv:1201.0753 [astro-ph.HE].
- [25] M. Ackermann *et al.* (Fermi-LAT), *Astrophys. J.* **812**, 159 (2015), arXiv:1510.00004 [astro-ph.HE].
- [26] X. Tan, M. Colavincenzo, and S. Ammazzalorso, *Mon. Not. Roy. Astron. Soc.* **495**, 114 (2020), arXiv:1907.06905 [astro-ph.CO].
- [27] C. Thorpe-Morgan, D. Malyshev, C.-A. Stegen, A. Santangelo, and J. Jochum, *Mon. Not. Roy. Astron. Soc.* **502**, 4039 (2021), arXiv:2010.11006 [astro-ph.HE].
- [28] M. Di Mauro, J. Pérez-Romero, M. A. Sánchez-Conde, and N. Fornengo, *Phys. Rev. D* **107**, 083030 (2023), arXiv:2303.16930 [astro-ph.HE].
- [29] D. Song, K. Murase, and A. Kheirandish, *JCAP* **03**, 024 (2024), arXiv:2308.00589 [astro-ph.HE].
- [30] G. Steigman, B. Dasgupta, and J. F. Beacom, *Phys. Rev. D* **86**, 023506 (2012), arXiv:1204.3622 [hep-ph].
- [31] A. McDaniel, M. Ajello, C. M. Karwin, M. Di Mauro, A. Drlica-Wagner, and M. A. Sánchez-Conde, *Phys. Rev. D* **109**, 063024 (2024), arXiv:2311.04982 [astro-ph.HE].
- [32] M. S. Delos, M. Korsmeier, A. Widmark, C. Blanco, T. Linden, and S. D. M. White, *Phys. Rev. D* **109**, 083512 (2024), arXiv:2307.13023 [astro-ph.HE].
- [33] F. Calore, I. Cholis, and C. Weniger, *JCAP* **03**, 038 (2015), arXiv:1409.0042 [astro-ph.CO].
- [34] D. Hooper and L. Goodenough, *Phys. Lett. B* **697**, 412 (2011), arXiv:1010.2752 [hep-ph].
- [35] D. Hooper and T. Linden, *Phys. Rev. D* **84**, 123005 (2011), arXiv:1110.0006 [astro-ph.HE].
- [36] K. N. Abazajian and M. Kaplinghat, *Phys. Rev. D* **86**, 083511 (2012), [Erratum: *Phys. Rev. D* **87**, 129902 (2013)], arXiv:1207.6047 [astro-ph.HE].
- [37] T. Daylan, D. P. Finkbeiner, D. Hooper, T. Linden, S. K. N. Portillo, N. L. Rodd, and T. R. Slatyer, *Phys. Dark Univ.* **12**, 1 (2016), arXiv:1402.6703 [astro-ph.HE].
- [38] F. Calore, I. Cholis, C. McCabe, and C. Weniger, *Phys. Rev. D* **91**, 063003 (2015), arXiv:1411.4647 [hep-ph].
- [39] M. Ackermann *et al.* (Fermi-LAT), *Astrophys. J.* **840**, 43 (2017), arXiv:1704.03910 [astro-ph.HE].
- [40] R. K. Leane and T. R. Slatyer, *Phys. Rev. Lett.* **123**, 241101 (2019), arXiv:1904.08430 [astro-ph.HE].
- [41] M. Di Mauro, *Phys. Rev. D* **103**, 063029 (2021), arXiv:2101.04694 [astro-ph.HE].
- [42] A. A. Abdo *et al.* (Fermi-LAT), *Astrophys. J.* **712**, 147 (2010), arXiv:1001.4531 [astro-ph.CO].
- [43] M. Ackermann *et al.* (Fermi-LAT), *Phys. Rev. D* **89**, 042001 (2014), arXiv:1310.0828 [astro-ph.HE].
- [44] A. Geringer-Sameth, S. M. Koushiappas, and M. G. Walker, *Phys. Rev. D* **91**, 083535 (2015), arXiv:1410.2242 [astro-ph.CO].
- [45] A. Geringer-Sameth, S. M. Koushiappas, and M. Walker, *Astrophys. J.* **801**, 74 (2015), arXiv:1408.0002 [astro-ph.CO].
- [46] M. Ackermann *et al.* (Fermi-LAT), *Phys. Rev. Lett.* **115**, 231301 (2015), arXiv:1503.02641 [astro-ph.HE].
- [47] S. Li, Y.-F. Liang, K.-K. Duan, Z.-Q. Shen, X. Huang, X. Li, Y.-Z. Fan, N.-H. Liao, L. Feng, and J. Chang, *Phys. Rev. D* **93**, 043518 (2016), arXiv:1511.09252 [astro-ph.HE].
- [48] A. Albert *et al.* (Fermi-LAT, DES), *Astrophys. J.* **834**, 110 (2017), arXiv:1611.03184 [astro-ph.HE].
- [49] A. Chiappo, J. Cohen-Tanugi, J. Conrad, and L. E. Strigari, *Mon. Not. Roy. Astron. Soc.* **488**, 2616 (2019), arXiv:1810.09917 [astro-ph.GA].

- [50] S. Hoof, A. Geringer-Sameth, and R. Trotta, *JCAP* **02**, 012 (2020), arXiv:1812.06986 [astro-ph.CO].
- [51] S. Li *et al.*, *Phys. Rev. D* **97**, 122001 (2018), arXiv:1805.06612 [astro-ph.HE].
- [52] F. Calore, P. D. Serpico, and B. Zaldivar, *JCAP* **10**, 029 (2018), arXiv:1803.05508 [astro-ph.HE].
- [53] A. Alvarez, F. Calore, A. Genina, J. Read, P. D. Serpico, and B. Zaldivar, *JCAP* **09**, 004 (2020), arXiv:2002.01229 [astro-ph.HE].
- [54] T. Linden, *Phys. Rev. D* **101**, 043017 (2020), arXiv:1905.11992 [astro-ph.HE].
- [55] S. Li, Y.-F. Liang, and Y.-Z. Fan, *Phys. Rev. D* **104**, 083037 (2021), arXiv:2110.01157 [astro-ph.HE].
- [56] M. Crnogorčević and T. Linden, *Phys. Rev. D* **109**, 083018 (2024), arXiv:2311.14611 [astro-ph.HE].
- [57] R. K. Sheth, H. J. Mo, and G. Tormen, *Mon. Not. Roy. Astron. Soc.* **323**, 1 (2001), arXiv:astro-ph/9907024.
- [58] A. V. Maccio, S. Paduroiu, D. Anderhalden, A. Schneider, and B. Moore, *Mon. Not. Roy. Astron. Soc.* **424**, 1105 (2012), arXiv:1202.1282 [astro-ph.CO].
- [59] J. Stücker, G. Ogiya, S. D. M. White, and R. E. Angulo, *Mon. Not. Roy. Astron. Soc.* **523**, 1067 (2023), arXiv:2301.04670 [astro-ph.CO].
- [60] J. M. Bardeen, J. R. Bond, N. Kaiser, and A. S. Szalay, *Astrophys. J.* **304**, 15 (1986).
- [61] D. Blas, J. Lesgourgues, and T. Tram, *JCAP* **07**, 034 (2011), arXiv:1104.2933 [astro-ph.CO].
- [62] N. Aghanim *et al.* (Planck), *Astron. Astrophys.* **641**, A6 (2020), [Erratum: *Astron. Astrophys.* 652, C4 (2021)], arXiv:1807.06209 [astro-ph.CO].
- [63] W. Hu and N. Sugiyama, *Astrophys. J.* **471**, 542 (1996), arXiv:astro-ph/9510117.
- [64] E. Bertschinger, *Phys. Rev. D* **74**, 063509 (2006), arXiv:astro-ph/0607319.
- [65] J. Stücker, G. Ogiya, R. E. Angulo, A. Aguirre-Santaella, and M. A. Sánchez-Conde, *Mon. Not. Roy. Astron. Soc.* **521**, 4432 (2023), arXiv:2207.00604 [astro-ph.CO].
- [66] M. Ackermann *et al.* (Fermi-LAT), *JCAP* **09**, 008 (2015), arXiv:1501.05464 [astro-ph.CO].
- [67] J. M. Cornell, S. Profumo, and W. Shepherd, *Phys. Rev. D* **88**, 015027 (2013), arXiv:1305.4676 [hep-ph].
- [68] W. B. Atwood *et al.*, *The Astrophysical Journal* **697**, 1071–1102 (2009).
- [69] M. Wood, R. Caputo, E. Charles, M. D. Mauro, J. Magill, and J. Perkins, “Fermipy: An open-source python package for analysis of fermi-lat data,” (2017), arXiv:1707.09551 [astro-ph.IM].
- [70] M. Cirelli, G. Corcella, A. Hektor, G. Hutsi, M. Kadastik, P. Panci, M. Raidal, F. Sala, and A. Strumia, *JCAP* **03**, 051 (2011), [Erratum: *JCAP* 10, E01 (2012)], arXiv:1012.4515 [hep-ph].
- [71] D. J. Bartlett, A. Kostić, H. Desmond, J. Jasche, and G. Lavaux, *Phys. Rev. D* **106**, 103526 (2022), arXiv:2205.12916 [astro-ph.CO].
- [72] Astropy Collaboration, *ApJ* **935**, 167 (2022), arXiv:2206.14220 [astro-ph.IM].
- [73] C. R. Harris, K. J. Millman, S. J. van der Walt, R. Gommers, P. Virtanen, D. Cournapeau, E. Wieser, J. Taylor, S. Berg, N. J. Smith, R. Kern, M. Picus, S. Hoyer, M. H. van Kerkwijk, M. Brett, A. Haldane, J. F. del Río, M. Wiebe, P. Peterson, P. Gérard-Marchant, K. Sheppard, T. Reddy, W. Weckesser, H. Abbasi, C. Gohlke, and T. E. Oliphant, *Nature* **585**, 357 (2020).
- [74] J. D. Hunter, *Computing in Science & Engineering* **9**, 90 (2007).
- [75] T. pandas development team, “pandas-dev/pandas: Pandas,” (2020).
- [76] L. M. Widrow, *ApJS* **131**, 39 (2000).